Contact time on curved superhydrophobic surfaces

Jeonghoon Han,[1] Wonjung Kim,[2] Changwoo Bae,[1] Dongwook Lee,[3] Seungwon Shin,[3] Youngsuk Nam,[1,*] and Choongyeop Lee[1,†]

[1]*Department of Mechanical Engineering, Kyung Hee University, Yongin 17104, Republic of Korea*

[2]*Department of Mechanical Engineering, Sogang University, Seoul 04107, Republic of Korea*

[3]*Department of Mechanical and System Design Engineering, Hongik University, Seoul 04066, Republic of Korea*

(Received 25 September 2019; revised manuscript received 19 March 2020; accepted 25 March 2020; published 24 April 2020)

When a water drop impinges on a flat superhydrophobic surface, it bounces off the surface after a certain dwelling time, which is determined by the Rayleigh inertial-capillary timescale. Recent works have demonstrated that this dwelling time (i.e., contact time) is modified on curved superhydrophobic surfaces, as the drop asymmetrically spreads over the surface. However, the contact time on the curved surfaces still remains poorly understood, while no successful physical model for the contact time has been proposed. Here, we propose that the asymmetric spreading on the curved surface is driven by either the Coanda effect or inertia depending on the ratio of the drop diameter to the curvature diameter. Then, based on scaling analysis, we develop the contact time model that successfully predicts the contact time measured under a wide range of experiment conditions such as different impact velocities and curvature diameters. We believe that our results illuminate the underlying mechanism for the asymmetric spreading over the curved surface, while the proposed contact time model can be utilized for the design of superhydrophobic surfaces for various thermal applications, where the thermal exchange between the surface and the water drop occurs via a direct physical contact.

DOI: 10.1103/PhysRevE.101.043108

I. INTRODUCTION

Drop impact on solid surfaces has been studied for decades for its relevance to various natural processes and practical applications such as ink-jet printing [1–4] spray cooling [5–7], moisture harvesting [8], electrical energy harvesting [9], and even forensic science [10,11] and pathogen dispersal [12]. This classical problem recently attracted renewed interest from researchers, as the advancement of micro- and nanofabrication techniques enabled the precise control of surface properties including both surface wettability and surface roughness [13]. Particularly, inspired by natural surfaces such as lotus leaf, multifunctional superhydrophobic (SHPo) surfaces with an extreme liquid repellency have been engineered, finding their applications in frictional drag reduction [14,15], enhanced condensation [16–18], and anti-icing [19,20].

On SHPo surfaces having the minimal adhesion with water, it was shown that the contact time between the impinging water drop and the surface is determined by the Rayleigh inertial-capillary timescale, such as $\tau_0 \sim \sqrt{\rho D_0^3/\gamma}$, where ρ, γ, and D_0 are the liquid density, surface tension, and drop diameter, respectively [21]. However, the recent studies demonstrated that macroscopic surface structures, comparable with the water drop diameter, can modify the contact time below this Rayleigh timescale [21–29]. For example, pillars of submillimeter feature sizes can be placed on the surface to induce the intentional partial penetration of a water drop into surface structures after impact [28]. After the partial penetration, the drop deformation within pillars provides a sufficient restoring force to lift the drop off the surface prematurely, resulting in a pancakelike bouncing morphology. Also, macroscale structures such as ridges can induce a redistribution of drop volume into several lobes after impact [23,24]. The smaller effective water volume within each lobe leads to a reduced contact time, where the measured contact time matches with the prediction value based on the effective water volume [24]. Note that the contact time reduction can be effective in mitigating icing problems on the surface by delaying ice nucleation during the contact between the water drop and the surface. It was recently demonstrated that, by decreasing the contact time from 17 to 11.4 ms, ice nucleation could be prevented on the SHPo surface at −20 °C [26]. Also, after the contact time reduction by half, ice nucleation was delayed to a much lower temperature; while ice nucleation was observed on the flat SHPo surface at −9 °C, no ice nucleation was observed on the SHPo with the reduced contact time even at a lower surface temperature of −13.8 °C [30].

Recently, it has been shown that the contact time is also modified on the SHPo surfaces with curvature, as the drop spreads asymmetrically over the surface with a larger spreading diameter along the curvature (i.e., azimuthal direction) [27]. The curved SHPo surface is of interest in itself, as it is directly relevant to heat transfer applications such as tube-type heat exchanger [31]. Additionally, as demonstrated in recent studies, surface features with curvature can be easily embedded onto the flat surface to minimize the contact time [22,25]. In a pioneering work by Liu *et al.* [27], it was numerically shown that the asymmetric momentum distribution

*ysnam1@khu.ac.kr
†cylee@khu.ac.kr

becomes more pronounced with the decrease of the curvature diameter, although no physical mechanism was proposed for the asymmetric spreading. Another study demonstrated that the contact time is also influenced by the impact velocity in addition to the curvature diameter [22,25]. However, to date, no successful physical model, which can explain the influence of both the surface curvature and the impact velocity on the contact time, has been proposed, possibly due to the complex spreading dynamics of the water drop over the curved surface [22,25,27].

In this work, we build the physical model about the contact time on the curved SHPo surfaces based on scaling analysis. We capture a few distinguishing features of drop spreading dynamics on the cylindrical SHPo surfaces, while considering either the Coanda effect or inertia as the underlying mechanism for asymmetric spreading. Our contact time model shows excellent agreement with the measured contact time under different impact velocities and cylinder diameters obtained with two different drop sizes.

II. METHODS

A. Experimental method

Commercial copper cylinder with its diameter $D_c = 16$, 9, 6, 3, 1.6, and 0.8 mm was used for the experiment after the surface treatment. As shown in Fig. 1(a), copper oxide (CuO) nanostructures of a few hundred nanometers were grown on copper cylinders using a chemical dipping method [32,33], followed by a hydrophobic treatment with HDFS (1H,1H,2H,2H-perfluorodecyltrimethoxysilane, Sigma-Aldrich). The advancing (θ_{adv}) and receding (θ_{rec}) contact angles were measured to be $163 \pm 1^\circ$ and $161 \pm 1^\circ$ on the modified surface, confirming superhydrophobicity. The impact dynamics on a SHPo cylinder was recorded by using a high-speed camera (Phantom M110) at 6200 frames per second from two different views, in order to resolve spreading and retraction dynamics along both azimuthal and axial directions. In the present study, two different sizes of the dispensing tips were used to control the drop size, where the measured drop diameter was about 2.3 and 3 mm, respectively.

B. Numerical method

In the present study, the level contour reconstruction method, i.e., a front tracking type method explicitly tracking implicitly connected individual interface elements, was used, while the following single field formulation of the continuity and momentum equations was solved [34,35]:

$$\nabla \cdot \mathbf{u} = 0, \tag{1}$$

$$\rho\left(\frac{\partial \mathbf{u}}{\partial t} + \mathbf{u} \cdot \nabla \mathbf{u}\right) = -\nabla P + \rho \mathbf{g} + \nabla \cdot \mu(\nabla \mathbf{u} + \nabla \mathbf{u}^{\mathrm{T}}) + \mathbf{F}, \tag{2}$$

where $\mathbf{u}$ is the velocity vector, P the pressure, and $\mathbf{g}$ the gravitational acceleration, respectively. Material property fields have been described using the Heavisdie function, $I(\mathbf{x}, t)$, which varies from zero to one near the interface. The interface

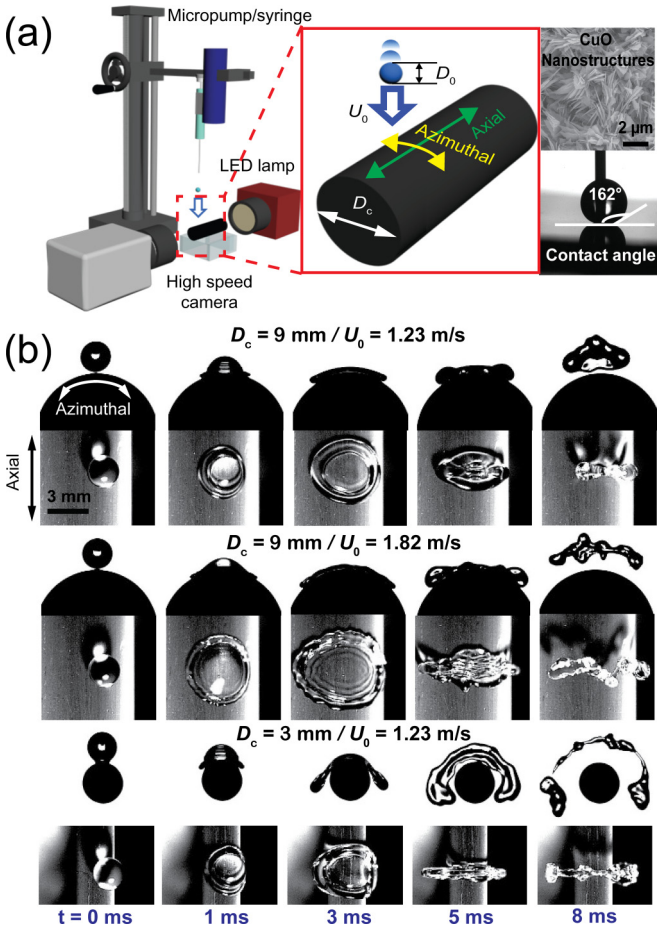

FIG. 1. (a) Schematic of drop impact experiment along with scanning electron microscopy image of CuO nanostructures and water contact angle. (b) Representative image sequences of drop impact dynamics of the water drop with $D_0 = 2.3$ mm on a superhydrophobic cylinder having the diameter D_c at the impact velocity U_0.

is advected in a Lagrangian fashion by integrating

$$\frac{d\mathbf{x}_f}{dt} = \mathbf{V}, \tag{3}$$

where $\mathbf{V}$ is the interface velocity vector interpolated at $\mathbf{x}_f$. The hybrid formulation with compact curvature support was used for the local surface tension force at the interface, $\mathbf{F}$. The detailed numerical process for solving the above governing equations can be found in the previous studies [34,35]. For contact line dynamic modeling, we used the generalized Navier-slip boundary condition [34] to account for the contact line behavior at the boundary wall, which allows contact line movement proportional to shear stress at the contact point. To account for contact angle hysteresis and static contact angle, we imposed that only when the contact angle θ is less or greater than the prescribed receding θ_{rec} or advancing angle θ_{adv}, the interface is free to move with the given receding or advancing contact angle, respectively. A more detailed treatment for the contact dynamics can be found elsewhere [36].

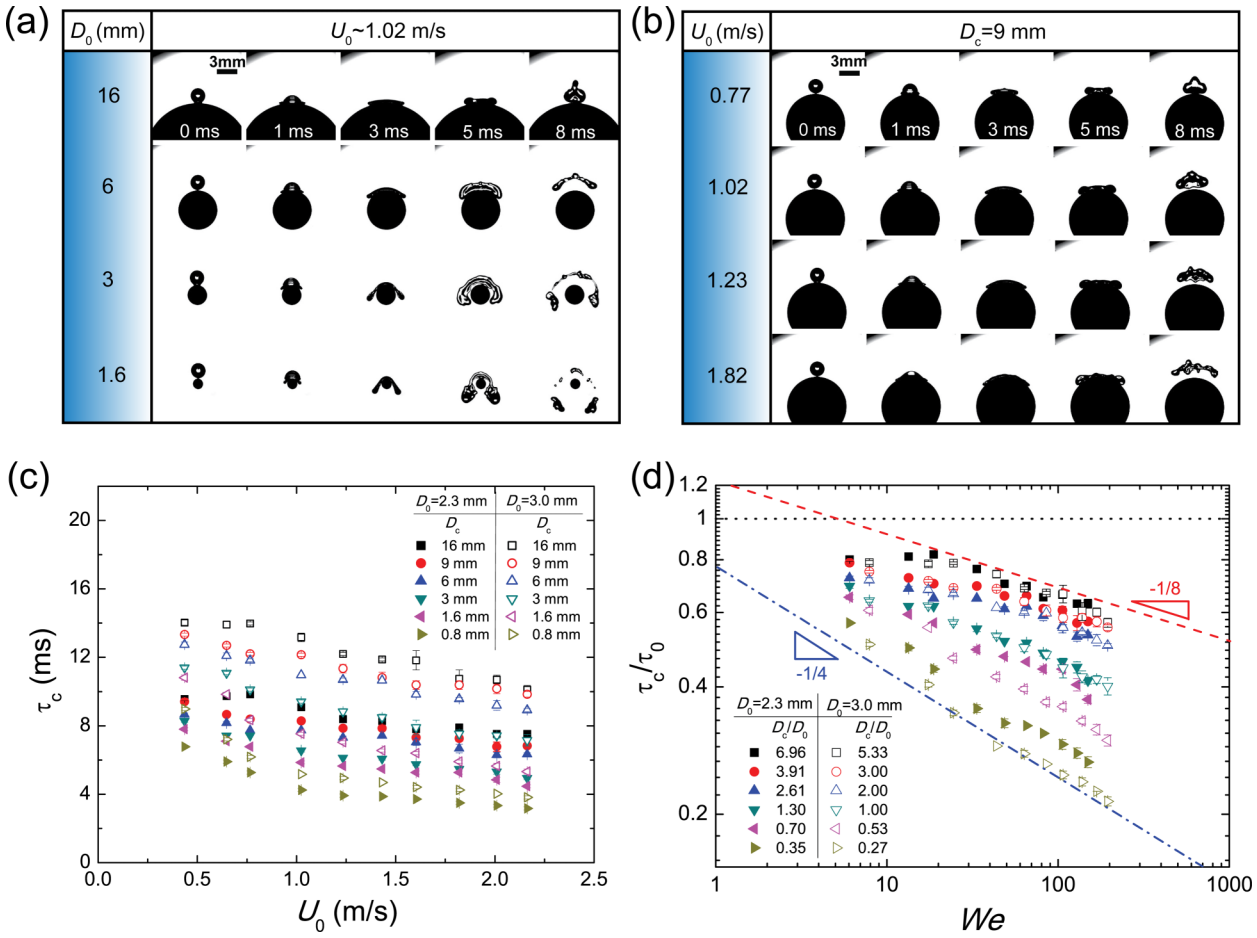

FIG. 2. Sequential images of the water drop ($D_0 = 2.3$ mm) after impact on a superhydrophobic cylinder, (a) as the cylinder diameter D_c varies at the fixed impact velocity U_0 of 1.02 m/s; and (b) as the impact velocity U_0 varies at the fixed cylinder diameter of $D_c = 9$ mm. (c) Measured contact time τ_c on a superhydrophobic cylinder as a function of the impact velocity U_0 and cylinder diameter D_c for two different drop diameters D_0 (2.3 and 3.0 mm). (d) Dimensionless contact time as a function of the We number and D_c/D_0.

III. EXPERIMENTAL RESULTS

Figure 1(b) shows the exemplary sequential images of dynamic behaviors of a water drop ($D_0 = 2.3$ mm) on the SHPo cylinder of the diameter D_c at the impact velocity of U_0 seen from two different angles. In agreement with the previous results [27], the water drop exhibits asymmetric spreading and retraction dynamics on the SHPo cylinder, such that the maximum spreading diameter is larger along the azimuthal direction than that along the axial direction. Figure 1(b) shows that the spreading diameter grows to become more asymmetric over time, while the asymmetry also appears to be influenced by the impact velocity U_0 and the cylinder diameter D_c. From Fig. 1(b), one can also see that after impact the drop spreading along the azimuthal direction tends to follow the contour of the surface. Notably, the spreading asymmetry is not manifest at ~1 ms. The spreading asymmetry appears to grow rapidly after ~3 ms, as spreading stops and reverses its direction along the axial direction, while the spreading diameter continues to increase along the azimuthal direction. Then, the drop bounces off the surface at the end of the retraction stage along the axial direction, where the earlier completion of the retraction stage results in a decrease of the contact time.

Figures 2(a) and 2(b) show the change of the drop impact dynamics along the azimuthal direction as well as the contact time, as the cylinder diameter D_c increases [Fig. 2(a)] or the impact velocity U_0 increases [Fig. 2(b)]. Both cases clearly show the contact time reduction with the increase of D_c and U_0. Figure 2(c) shows the experimentally measured contact time τ_c with the water drop of $D_0 = 2.3$ or 3.0 mm on the SHPo cylinders having the different diameter D_c as a function of the impact velocity U_0. Here, τ_c is defined as the contact time on the cylindrical surface. One can see that τ_c decreases monotonically, as the impact velocity U_0 increases or D_c decreases with the maximum contact time reduction by 60%–70% from its largest value. Also, τ_c is larger with the drop diameter $D_0 = 3.0$ mm over $D_0 = 2.3$ mm at the same U_0 and D_c.

Here, to understand the influence of the impact velocity U_0, the cylinder diameter D_c, and the drop diameter D_0 on the contact time τ_c, we nondimensionalize the relevant parameters as the following. First, as our study is limited to water with a low viscosity ($\mu = 0.001$ Pa s), we assume that the drop dynamics is mostly governed by inertial and capillary effect, parametrized by the Weber number $\mathrm{We} = \rho U_0^2 D_0/\gamma$ with the density $\rho = 1000\,\mathrm{kg/m^3}$ and the surface tension $\gamma = 72\,\mathrm{mN/m}$.. Note that the Reynolds number

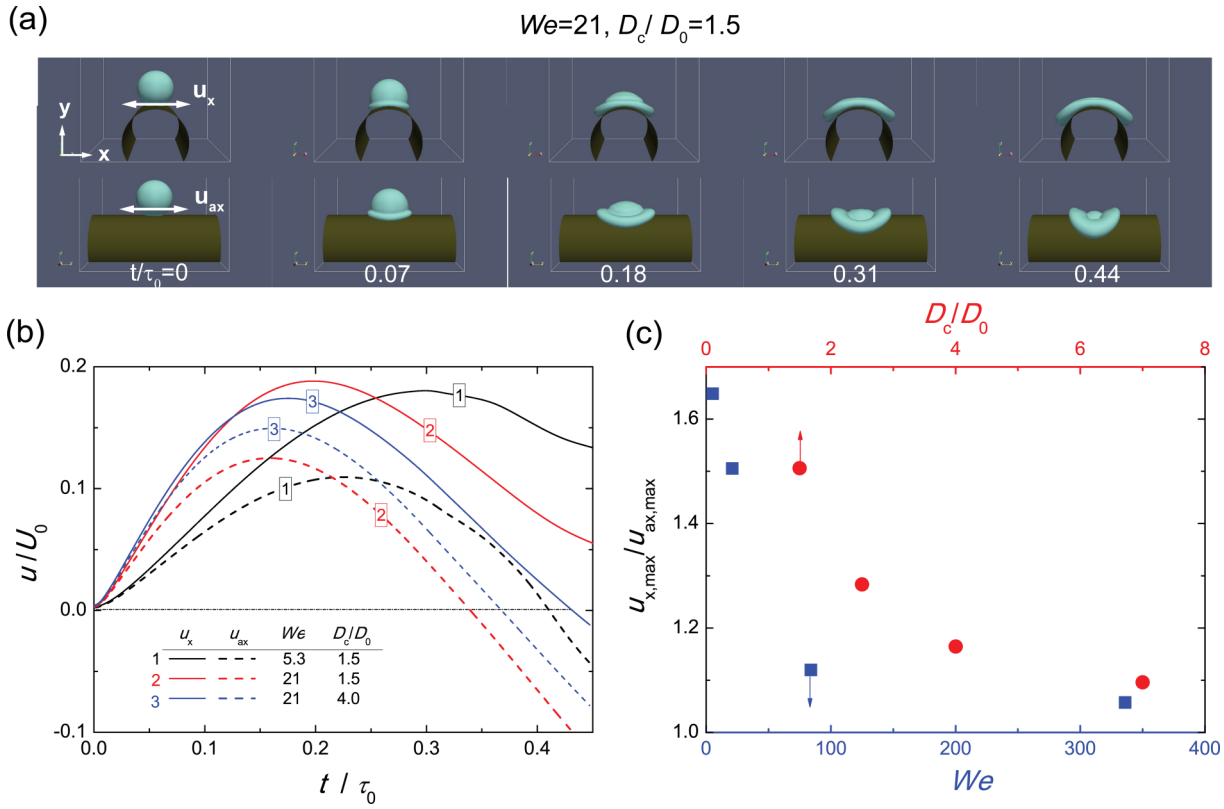

FIG. 3. (a) Simulated drop spreading dynamics at We = 21 on the cylinder with $D_c/D_0 = 1.5$. (b) The temporal change of the nondimensional averaged spreading velocity along and transverse to the axial direction when the We number and D_c/D_0 change. (b) The ratio of the maximum spreading velocity along and transverse to the axial direction as a function of D_c/D_0 at the We number of 21 (red circle), and as a function of the We number on the cylinder with $D_c/D_0 = 1.5$ (blue square).

$Re = \rho U_0 D_0/\mu$ in the present study is always >1000, justifying the neglect of viscous dissipation. Also, the cylinder diameter D_c is normalized by the drop diameter D_0, while the contact time τ_c is normalized with $\tau_0 = C\sqrt{\rho D_0^3/\gamma}$ with a proportionality constant $C = 0.92$ to match the contact time on the flat SHPo surface.

The normalized contact time τ_c/τ_0 is shown as a function of the We number and D_c/D_0 in a log-log plot in Fig. 2(d). In Fig. 2(d), one can see that τ_c/τ_0 approaches a unity, i.e., the value on the flat SHPo surface, as D_c/D_0 increases and We decreases. It is interesting to note that at the same We number, τ_c/τ_0 monotonically decreases with the decrease of D_c/D_0 regardless of the drop diameter D_0. Also, τ_c/τ_0 decreases more rapidly with the We number as D_c/D_0 decreases, implying the change of the relevant dynamics with the decrease of D_c/D_0.

IV. NUMERICAL RESULTS

Following the previous approach [27], we used the numerical simulation to investigate the development of asymmetric momentum distribution (i.e., velocity distribution) right after impact. Figure 3(a) shows the representative images of drop spreading dynamics on the cylindrical SHPo surface with $D_c/D_0 = 1.5$ at We = 21, exhibiting the qualitatively similar drop impact dynamics with the experimental results. Quantitatively, we extract the characteristic spreading velocity along the azimuthal direction and axial direction. Note that, along the azimuthal direction, it is not straightforward to define the spreading velocity u_{az}, as the spreading direction keeps changing both temporally and spatially within the drop. Particularly, the definition becomes more ambiguous when one tries to estimate the azimuthal velocity at the location away from the surface. Here, following the previous approach [27], we measure the velocity along the transverse direction to the axis of the cylinder [see Fig. 3(a)] at every point within the water drop, and average it over the whole drop volume to calculate the representative velocity u_x for the azimuthal velocity u_{az}. Meanwhile, by following the same procedure, we calculate u_{ax}, the average spreading velocity along the axial direction. From Fig. 3(b), which shows the temporal change of the average velocity with respect to U_0, one can see that u_x is always larger than u_{ax}, and the difference between the two grows gradually over time. Here, we extract the maximum spreading velocity $u_{x,max}$ and $u_{ax,max}$ for each simulation case and calculate its ratio to quantify the extent of the asymmetric spreading velocity along the two different directions [Fig. 3(c)]. As D_c decreases with respect to D_0, one can see that the velocity ratio increases, leading to more asymmetric spreading in agreement with the previous results [27]. However, when the We number increases, one can see that the velocity ratio *decreases* instead of *increases*, even though the contact time τ_c decreases with the We number. These results contrast with the change of D_c/D_0, where the velocity ratio correlates with the extent of the asymmetry. Therefore, at odds with the argument in [27], we can conclude that the asymmetric velocity (or momentum) distribution alone is

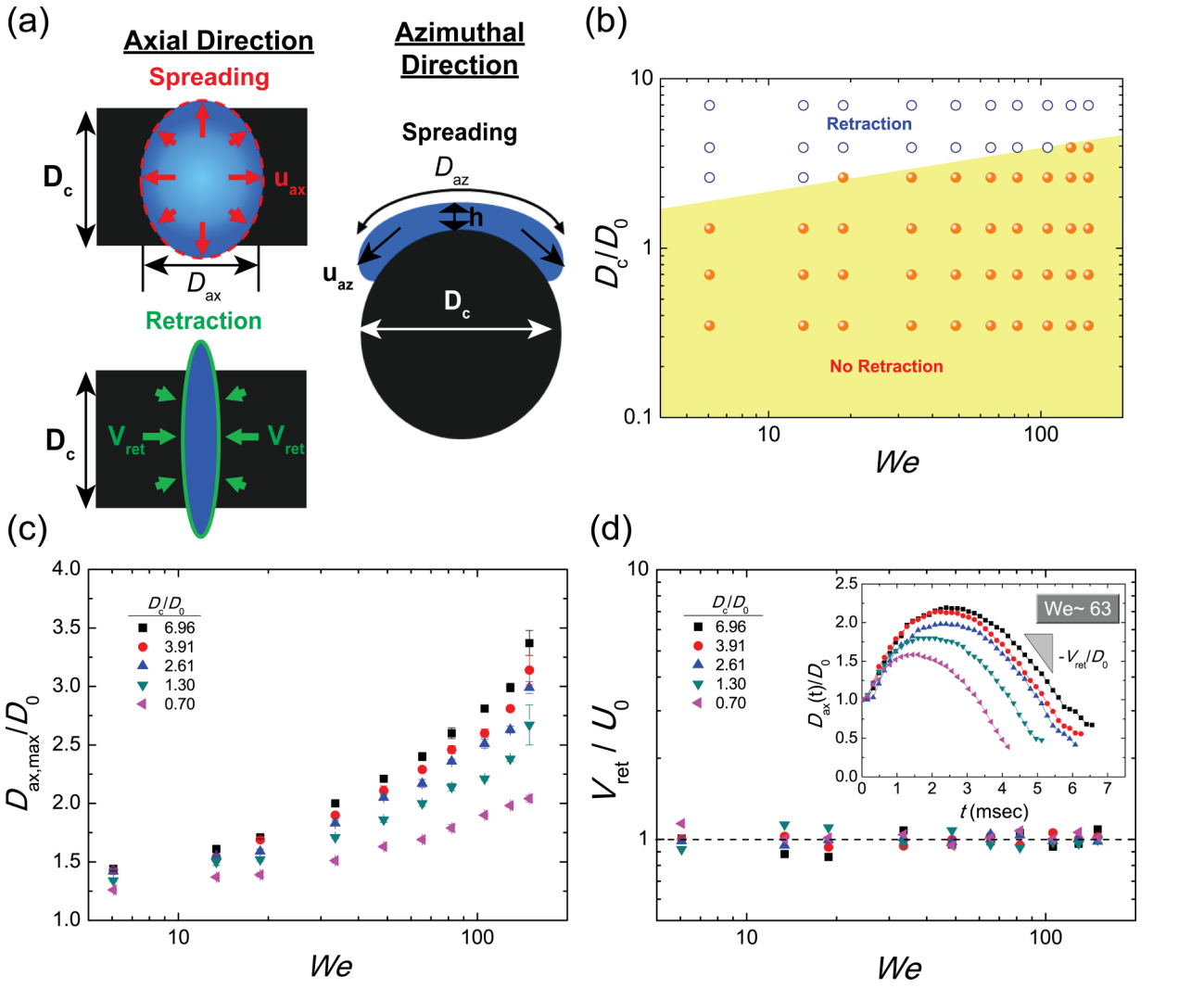

FIG. 4. (a) Schematic of drop impact dynamics on a cylindrical superhydrophobic surface. (b) Retraction regime along the azimuthal direction as a function of the We number and D_c/D_0 for the water drop with $D_0 = 2.3$ mm. (c) The maximum spreading ratio $D_{ax,max}/D_0$ along the axial direction as a function of the We number and D_c/D_0 for the water drop with $D_0 = 2.3$ mm. (d) Normalized retraction velocity along the axial direction as a function of the We number and D_c/D_0 for the water drop with $D_0 = 2.3$ mm. Inset shows the temporal change of the spreading diameter along the axial direction at We $\sim$ 63 for the different D_c/D_0.

insufficient in explaining the contact time reduction, as the We number and the cylinder diameter D_c affects the velocity asymmetry and the contact time in an opposite direction.

V. CONTACT TIME MODEL

Here, instead of relying on the asymmetric ratio of the maximum momentum along the axial and azimuthal directions, we attempt to capture unique features of drop impact dynamics over the SHPo cylinder from the experimental observations. As schematically illustrated in Fig. 4(a), the retraction dynamics of a water drop is often missing along the azimuthal direction, while this "no retraction" feature becomes more manifest at the smaller D_c/D_0 or larger We number [Fig. 4(b)]. This observation can be expressed as $D_{az,max} \sim u_{az}\tau_c$, where u_{az} is the spreading velocity along the azimuthal direction and $D_{az,max}$ is the maximum spreading diameter along the azimuthal direction.

As explained with Fig. 1(b), the contact time τ_c is mainly determined by the drop spreading and retraction dynamics along the axial direction. In Fig. 4(c), one can see that the smaller D_c/D_0 leads to the smaller maximum spreading ratio $D_{ax,max}/D_0$ along the axial direction, while the difference in $D_{ax,max}/D_0$ grows with the increase of the We number. Also, as shown in the inset of Fig. 4(d), the temporal change of the spreading diameter ratio $D_{ax}(t)/D_0$ along the axial direction indicates that the retraction velocity V_{ret}, i.e., the maximum velocity of contact line during retraction as schematically shown in the inset of Fig. 4(d), is nearly invariant with D_c/D_0. Normally, the retraction rate is determined by the Taylor-Culick formula $V_{ret} = \sqrt{2\gamma/\rho h}$ with h being the thickness of the flattened drop [37]. However, the rim formation at the edge of the spreading drop results in nonuniform thickness h, particularly at the high We number, making the Taylor-Culick approach inapplicable to the present case. Instead, if the dimensional analysis is applied to the functional relationship of $V_{ret} = f_1(U_0, D_0, D_c, \rho, \gamma)$, a

functional form of $V_{\rm ret}/U_0 = \phi_1(D_c/D_0, {\rm We})$ is obtained. Here, we experimentally find out that $V_{\rm ret}/U_0$ is independent of both D_c/D_0 and the We number as shown in Fig. 4(d), resulting in $V_{\rm ret}/U_0 \sim$ const for all experimental conditions. Then, as both the spreading and retraction velocity along the axial direction are scaled as U_0, one can write the contact time as $\tau_c \sim D_{\rm ax,max}/U_0$.

Additionally, the volume conservation dictates $D_0^3 \sim D_{\rm ax,max}D_{\rm az,max}h$, while the drop height h can be represented as $h \sim D_0{\rm We}^{-1/2}$, as h is determined by the effective capillary length $h \sim \sqrt{\gamma/\rho a}$ with the effective acceleration $a \sim U_0^2/D_0$ [38]. Then, τ_c can be alternatively expressed as $\tau_c \sim D_0^3/(D_{\rm az,max}hU_0) \sim {\rm We}^{1/2}D_0^2/(U_0D_{\rm az,max})$. With $D_{\rm az,max} \sim u_{\rm az}\tau_c$, one can obtain $\tau_c/\tau_0 \sim {\rm We}^{-1/4}\sqrt{U_0/u_{\rm az}}$ after nondimensionalizing τ_c with τ_0. To determine $U_0/u_{\rm az}$, an additional condition for $u_{\rm az}$ is necessary, while this condition needs to reflect the underlying mechanism for the preferential spreading along the azimuthal direction.

In Fig. 1(b), it is observed that the asymmetric spreading only begins to develop rapidly after ~3 ms. According to the theoretical study [39], the initial dynamic pressure decreases exponentially after impact. For example, the pressure at the center would be less than 2% of the initial value at ~3 ms for $D_0 = 2.3$ mm and $U_0 = 1$ m/s. This estimation implies that the preferential spreading along the azimuthal direction is manifest only after the initial dynamic pressure becomes negligible. Also, it should be noted that the drop spreads along the azimuthal direction following the contour of the curved surface. It is well known that the streamline of the liquid flow can follow the curved surface due to the Coanda effect [40,41]. In the Coanda effect, the bending of the streamlines at the curved surface creates the pressure drop at the surface, while the pressure drop can be estimated based on the Bernoulli theorem such as $\Delta P \sim -\rho U_0^2 h/D_c$ [40,41]. Here, we propose that this pressure drop is directly responsible for the preferential spreading along the azimuthal

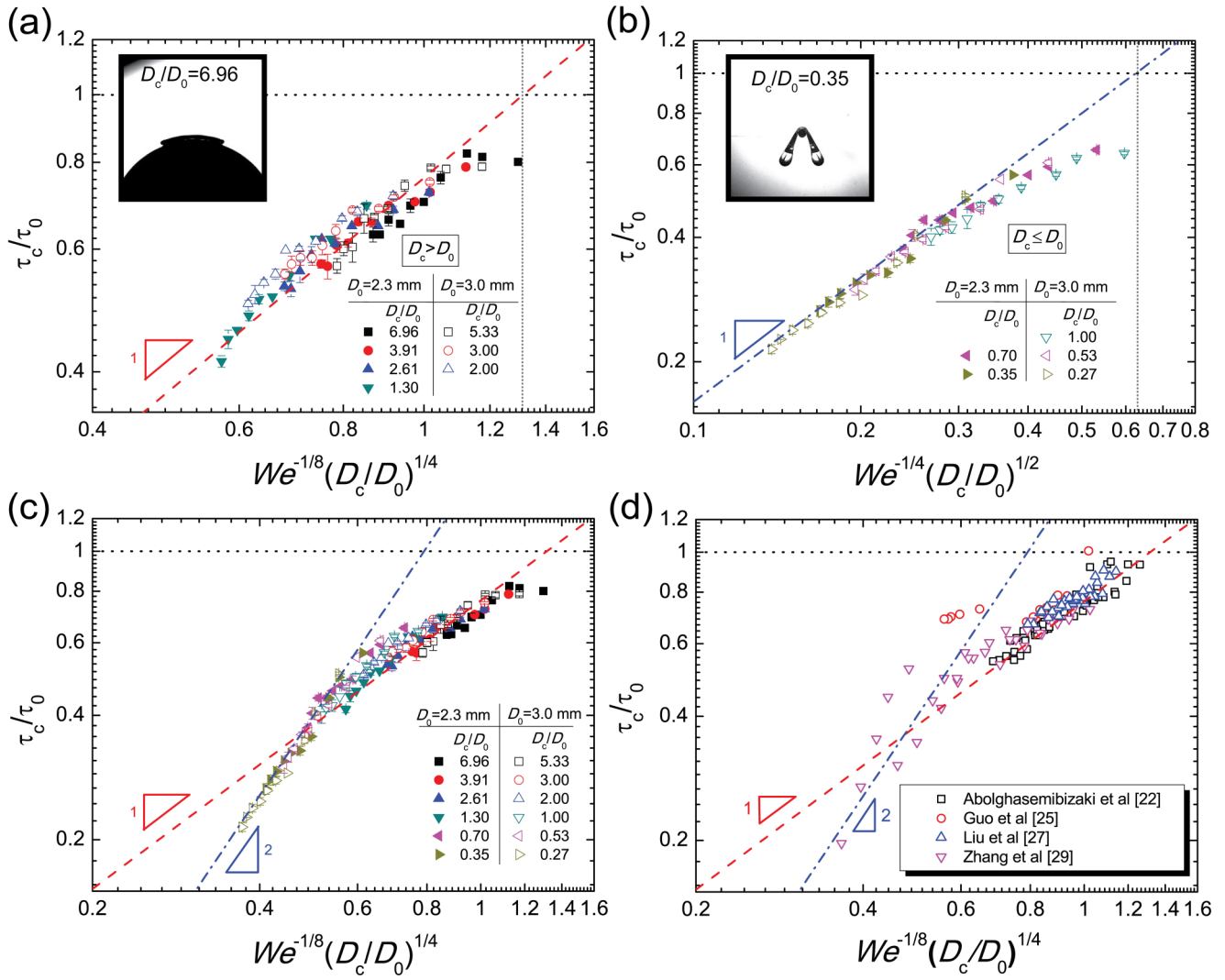

FIG. 5. Scaling relationship for the contact time on the superhydrophobic cylinder along with the experimental data. (a) Normalized contact time τ_c/τ_0 as a function of ${\rm We}^{-1/8}(D_c/D_0)^{1/4}$ for the experimental data with $D_c > D_0$. Inset: drop spreading image with $D_c/D_0 = 6.96$. (b) Normalized contact time τ_c/τ_0 as a function of ${\rm We}^{-1/4}(D_c/D_0)^{1/2}$ for the experimental data with $D_c \leqslant D_0$. Inset: drop spreading image with $D_c/D_0 = 0.35$. (c) Normalized contact time τ_c/τ_0 as a function of ${\rm We}^{-1/8}(D_c/D_0)^{1/4}$ for all the experimental data. (d) Comparison of the proposed contact time model with the experimental data from the previous works.

direction after the initial dynamic pressure decays. Then, from the momentum balance $\rho u\,\partial u/\partial \ell = -\partial P/\partial \ell$, one obtains $\rho u_{az}^2/\ell_{az} \sim \Delta P/\ell_{az} \sim \rho U_0^2 h/\ell_{az} D_c$ with ℓ_{az} being the characteristic length along the azimuthal direction, resulting in $u_{az}/U_0 \sim \mathrm{We}^{-1/4}\sqrt{D_0/D_c}$. With this velocity scaling, we obtain the scaling relation for the contact time such as $\tau_c/\tau_0 \sim \mathrm{We}^{-1/8}(D_c/D_0)^{1/4}$. However, as shown in Fig. 5(c), this scaling shows good agreement with the experimental data only for $0.48 < \mathrm{We}^{-1/8}(D_c/D_0)^{1/4} < 1.25$. For $\mathrm{We}^{-1/8}(D_c/D_0)^{1/4} < 0.48$, the measured contact time significantly deviates from this scaling, and the nondimensionalized contact time τ_c/τ_0 varies much more steeply with $\mathrm{We}^{-1/8}(D_c/D_0)^{1/4}$. However, if one considers only the cases with $D_c > D_0$, the data collapse into a single graph with the expected scaling exponent and proportionality coefficient on the order of unity such as $\tau_c/\tau_0 \approx 0.76\,\mathrm{We}^{-1/8}(D_c/D_0)^{1/4}$, as shown in Fig. 5(a). The deviation of the proposed scaling for the cases with $D_c < D_0$ indicates the presence of an additional physical mechanism at play. Indeed, in Fig. 2(d), it is observed that τ_c/τ_0 decreases much faster with the We number for smaller D_c/D_0. For $D_c < D_0$, a non-negligible portion of the water drop is located outside the SHPo cylinder, and it would preserve some of its inertia even after impact on the cylinder. Then, this inertia would be directly responsible for the preferential spreading along the azimuthal direction. Going back to the foregoing scaling relationship $\tau_c/\tau_0 \sim \mathrm{We}^{-1/4}\sqrt{U_0/u_{az}}$, one obtains $\tau_c/\tau_0 \sim \mathrm{We}^{-1/4}$, as the characteristic velocity u_{az} is scaled as U_0, i.e., the characteristic velocity outside the cylinder. Then, we recover the observed scaling with the We number in Fig. 2(d) for the smaller D_c/D_0, although this scaling still does not account for the influence of D_c/D_0. This deficiency can be addressed by considering additional modification. Due to the presence of a non-negligible portion of the water drop outside the cylinder, the effective water volume on the cylinder would be modified from $V_0 \sim D_0^3$ to $V_{0,e} \sim D_c D_0^2$, resulting in the effective drop diameter $D_{0,e} \sim (D_c D_0^2)^{1/3}$. Accordingly, the inertial-capillary timescale would be modified to be $\tau_{0,e} \sim \sqrt{\rho D_{0,e}^3/\gamma} \sim \sqrt{D_c/D_0}\sqrt{\rho D_0^3/\gamma} \sim \sqrt{D_c/D_0}\tau_0$. If one rewrites the contact time using the modified inertial-capillary time such as $\tau_c/\tau_{0,e} \sim \mathrm{We}^{-1/4}$, one finally obtains $\tau_c/\tau_0 \sim \mathrm{We}^{-1/4}(D_c/D_0)^{1/2}$. As shown in Fig. 5(b), the experimental data for the cases with $D_c \leqslant D_0$ agree well with the proposed scaling relationship with a proportionality constant on the order of unity such as $\tau_c/\tau_0 \approx 1.59\,\mathrm{We}^{-1/4}(D_c/D_0)^{1/2}$. Here, the deviation from the proposed scaling relationship is observed for the case with $D_c/D_0 = 1$ at the smaller We number, as the Coanda effect becomes more relevant.

Finally, in Fig. 5(c), one can observe that the contact time reduction on the SHPo cylinder can be well represented by the proposed scaling relationships and can be roughly divided into the following two regimes depending on a single parameter $\mathrm{We}^{-1/8}(D_c/D_0)^{1/4}$.

I: $\tau_c/\tau_0 \approx 0.76\,\mathrm{We}^{-1/8}(D_c/D_0)^{1/4}$ for $0.48 < \mathrm{We}^{-1/8}(D_c/D_0)^{1/4} < 1.25$

II: $\tau_c/\tau_0 \approx 1.59\,\mathrm{We}^{-1/4}(D_c/D_0)^{1/2}$ for $\mathrm{We}^{-1/8}(D_c/D_0)^{1/4} < 0.48$.

For regime I, the Coanda effect is the underlying cause for the preferential spreading along the azimuthal direction, while the contact time reduction is the ramification of the asymmetric spreading. For regime II, the water volume outside the cylinder is the underlying cause for the modification of the contact time by inducing the asymmetric spreading with its inertia as well as the reduction in the effective water volume on the cylinder. Here, the transition from regime I to regime II is dependent on the We number as well as D_c/D_0, as the higher *We* number would increase the drop spreading diameter over the cylinder, thus effectively decreasing the ratio of the cylinder diameter to the drop diameter during impact. Figure 5(d) shows good agreement with the proposed contact time model with the experimental data from the previous studies [22,25,27,29], validating the proposed model.

VI. CONCLUSIONS

In summary, we developed a scaling model for the contact time of the water drop on curved superhydrophobic surfaces. Despite our simple scaling approach to the complex drop dynamics on the curved surface, our contact time model demonstrated good agreement with the measured contact time under a wide range of impact conditions such as different surface curvatures and impact velocities, for two different drop diameters. Also, with its simple functional form, our physical model would be easily implemented to various thermal applications involving curved surfaces such as transmission lines and high voltage insulators, where reducing the contact time can be an effective strategy to minimize the thermal exchange between the surface and the water drops.

ACKNOWLEDGMENTS

This work was supported by Basic Science Research Program (2020R1A2C1010767, 2019R1A2C2004607, 2017R1D1A1B03028518) through the National Research Foundation of Korea (NRF) funded by the Ministry of Science and ICT and the Ministry of Education.

[1] U.-C. Yi and C.-J. Kim, Sens. Actuators A **114**, 347 (2004).
[2] H. Wijshoff, Curr. Opin. Colloid Interface Sci. **36**, 20 (2018).
[3] Y. Zhang, T. Ren, and J. He, ACS Appl. Mater. Interfaces **10**, 11343 (2018).
[4] H. Shahariar, I. Kim, H. Soewardiman, and J. S. Jur, ACS Appl. Mater. Interfaces **11**, 6208 (2019).
[5] J. Breitenbach, I. V. Roisman, and C. Tropea, Int. J. Heat Mass Transfer **110**, 34 (2017).
[6] J. Breitenbach, I. V. Roisman, and C. Tropea, Exp. Fluids **59**, 55 (2018).
[7] M. Ciofalo, A. Caronia, M. Di Liberto, and S. Puleo, Int. J. Heat Mass Transfer **50**, 4948 (2007).
[8] M. Damak and K. K. Varanasi, Sci. Adv. **4**, eaao5323 (2018).

[9] Y. Xie, D. Bos, L. J. de Vreede, H. L. de Boer, M.-J. van der Meulen, M. Versluis, A. J. Sprenkels, A. van den Berg, and J. C. T. Eijkel, Nat. Commun. **5**, 3575 (2014).
[10] F. R. Smith, C. Nicloux, and D. Brutin, Phys. Rev. Fluids **3**, 013601 (2018).
[11] N. Laan, K. G. de Bruin, D. Slenter, J. Wilhelm, M. Jermy, and D. Bonn, Sci. Rep. **5**, 11461 (2015).
[12] S. Kim, H. Park, H. A. Gruszewski, D. G. Schmale, and S. Jung, Proc. Natl. Acad. Sci. USA **116**, 4917 (2019).
[13] C. Josserand and S. T. Thoroddsen, Annu. Rev. Fluid Mech. **48**, 365 (2016).
[14] C. Lee, C.-H. Choi, and C.-J. "CJ" Kim, Phys. Rev. Lett. **101**, 064501 (2008).
[15] C. Lee, C.-H. Choi, and C.-J. Kim, Exp. Fluids **57**, 176 (2016).
[16] N. Miljkovic, R. Enright, Y. Nam, K. Lopez, N. Dou, J. Sack, and E. N. Wang, Nano Lett. **13**, 179 (2013).
[17] D. Xing, F. Wu, R. Wang, J. Zhu, and X. Gao, ACS Appl. Mater. Interfaces **11**, 7553 (2019).
[18] D. Seo, J. Shim, B. Moon, K. Lee, J. Lee, C. Lee, and Y. Nam, ACS Appl. Mater. Interfaces **12**, 4068 (2020).
[19] D. Seo, S. Oh, B. Moon, H. Kim, J. Kim, C. Lee, and Y. Nam, Int. J. Heat Mass Transfer **128**, 217 (2019).
[20] Z. Zuo, R. Liao, C. Guo, Y. Yuan, X. Zhao, A. Zhuang, and Y. Zhang, Appl. Surf. Sci. **331**, 132 (2015).
[21] D. Richard, C. Clanet, and D. Quéré, Nature (London) **417**, 811 (2002).
[22] M. Abolghasemibizaki, R. L. McMasters, and R. Mohammadi, J. Colloid Interface Sci. **521**, 17 (2018).
[23] J. C. Bird, R. Dhiman, H.-M. Kwon, and K. K. Varanasi, Nature (London) **503**, 385 (2013).
[24] A. Gauthier, S. Symon, C. Clanet, and D. Quéré, Nat. Commun. **6**, 8001 (2015).
[25] C. Guo, J. Sun, Y. Sun, M. Wang, and D. Zhao, Appl. Phys. Lett. **112**, 263702 (2018).
[26] S.-H. Lee, M. Seong, M. K. Kwak, H. Ko, M. Kang, H. W. Park, S. M. Kang, and H. E. Jeong, ACS Nano **12**, 10693 (2018).
[27] Y. Liu, M. Andrew, J. Li, J. M. Yeomans, and Z. Wang, Nat. Commun. **6**, 10034 (2015).
[28] Y. Liu, L. Moevius, X. Xu, T. Qian, J. M. Yeomans, and Z. Wang, Nat. Phys. **10**, 515 (2014).
[29] H. Zhang, X. Yi, Y. Du, R. Zhang, X. Zhang, F. He, F. Niu, and P. Hao, Phys. Fluids **31**, 032104 (2019).
[30] T. Vasileiou, T. M. Schutzius, and D. Poulikakos, Langmuir **33**, 6708 (2017).
[31] D. Seo, J. Lee, C. Lee, and Y. Nam, Sci. Rep. **6**, 24276 (2016).
[32] J. Han, S. Ryu, H. Kim, P. Sen, D. Choi, Y. Nam, and C. Lee, Soft Matter **14**, 3760 (2018).
[33] Y. Nam and Y. S. Ju, J. Adhes. Sci. Technol. **27**, 2163 (2013).
[34] S. Shin and D. Juric, J. Comput. Phys. **180**, 427 (2002).
[35] S. Shin and D. Juric, Int. J. Numer. Methods Fluids **60**, 753 (2009).
[36] S. Shin, J. Chergui, and D. Juric, Theor. Comput. Fluid Dyn. **32**, 655 (2018).
[37] D. Bartolo, C. Josserand, and D. Bonn, J. Fluid Mech. **545**, 329 (2005).
[38] C. Clanet, C. Béguin, D. Richard, and D. Quéré, J. Fluid Mech. **517**, 199 (2004).
[39] I. V. Roisman, E. Berberović, and C. Tropea, Phys. Fluids **21**, 052103 (2009).
[40] C. Duez, C. Ybert, C. Clanet, and L. Bocquet, Phys. Rev. Lett. **104**, 084503 (2010).
[41] E. Jambon-Puillet, W. Bouwhuis, J. H. Snoeijer, and D. Bonn, Phys. Rev. Lett. **122**, 184501 (2019).